Growth of multilayer ice films and the formation of cubic ice imaged with STM

Konrad Thürmer and Norman C. Bartelt
Sandia National Laboratories, Livermore, California 94550, USA
(Received 31 December 2007; revised manuscript received 13 March 2008; published 16 May 2008)

Ice films as many as 30 molecular layers thick can be imaged with scanning tunneling microscopy (STM) when negative sample biases $<-6(\pm 1)$ V and subpicoamp tunneling currents are used. We observe that water deposited onto Pt(111) below 120 K forms amorphous films, whereas metastable cubic ice appears between 120 and 150 K. To determine the mechanisms of ice growth, we investigate the thickness-dependent film morphology. Cubic ice emerges from screw dislocations in the crystalline ice film that are caused by the mismatch in the atomic Pt- step height and the ice-bilayer separation.

DOI: 10.1103/PhysRevB.77.195425 PACS number(s): 68.55.−a, 68.37.Ef

I. INTRODUCTION

Many naturally occurring processes[1–3] are influenced by how ice grows on solid substrates. As is true for other materials systems,[4] the essential properties of crystalline ice films are often decided during the initial stages of growth. Thus, imaging the first molecular layers as they grow can provide the key to understanding the factors that determine the film's morphology and structure. In this pursuit, there have been several scanning tunneling microscopy (STM) observations at low temperatures in UHV of the first one or two layers of ice,[5–7] and, very recently, of ≈1 nm high ice clusters that nucleated from annealed amorphous ice.[8] Still, the nanometer-thickness range has eluded examination by microscopy, and important questions about multilayer ice growth remain, such as, e.g., why cubic ice often forms instead of hexagonal ice. The extreme sensitivity of ice to electron beam damage severely hampers the use of electron microscopy,[9,10] and x-ray topography with nanometer resolution has not been reported.[10] STM has not yet been applied to ice multilayer growth, perhaps because of the perception that the insulating character of ice prevents maintaining an electric current high enough to sustain the imaging process or that these currents will damage the film. Here, we report how these constraints can be overcome and how STM can be used to gain insights into how ice grows on Pt(111).

Many techniques[6,11–17] have been used to investigate ice on Pt(111). It is commonly accepted that ice films grow amorphous below 120 K and crystalline at higher temperatures. Although most studies agree that the equilibrium structure consists of isolated three-dimensional ice crystals on the Pt surface covered by a bilayer of water molecules, there is less agreement about the exact growth morphology of crystalline ice multilayers. For example, M. Morgenstern *et al.*[6] reported second layer nucleation for 140 K on every unit cell of the wetting layer, i.e., ≈3 nm apart, whereas the thermal-desorption experiments of Kimmel *et al.*[18] suggest that the wetting layer is covered by much larger, well separated three-dimensional islands. Here, we report that STM can track the growth of amorphous and crystalline ice multilayers, revealing how film morphology evolves with thickness. Such detailed topographic information provides new insights into the mechanisms of multilayer ice growth. For example, a common but not well understood observation is that ice grows at temperatures between 120 and 150 K in its metastable cubic 1c variant rather than in its equilibrium hexagonal form ice 1h.[1,2,19–21] We find evidence for ice 1c in thicker films and suggest that it is a consequence of the difficulty to nucleate new molecular layers on top of a growing crystal. We propose a mechanism of cubic ice formation via growth spirals around screw dislocations and show that these dislocations are generated by the mismatch in the atomic Pt-step height and the ice-bilayer separation.

II. EXPERIMENT

Our experiments were performed in a UHV chamber with a base pressure of $<3\times10^{-11}$ mbar. The ice films were grown at a rate of 1 Å/min by directing water vapor onto the cooled platinum sample. During water deposition, the STM tip was retracted far from the sample to exclude tip-induced modifications of the film growth. After each deposition, a small nonevaporable getter pump in the line of sight to the sample surface was added to accelerate pressure recovery. The sample was then cooled to imaging temperatures between 100 and 120 K. The crystallographic directions of the substrate were determined by evaluating the registry of atomic positions on both sides of an atomic Pt step. All STM images herein are oriented with respect to the Pt(111) crystallographic directions in the same way. For imaging, we used a negative sample bias $V_{\text{sample}}<-6(\pm 1)$ V and a small tunneling current $I_t\approx 0.4$ pA. At these conditions, we were able to routinely acquire images that show no sign of tip-induced film damage, whereas larger currents and, in particular, sample voltages $V_{\text{sample}}>-6(\pm 1)$ V destroy multilayer ice films in a very obvious way (see Sec. V). The image of a 4 nm thick ice film in Fig. 1, which shows surface steps with a bilayer height (3.7 Å), illustrates STM's capability to nondestructively examine ice multilayers. In Sec. V, we propose a tentative explanation for this unexpected ability to image thicker ice.

III. GROWTH OF AMORPHOUS AND CRYSTALLINE ICE MULTILAYERS

In this section we present a survey of the growth of ice multilayers on Pt(111) at different temperatures. We are able to image in real space what has been obtained before by

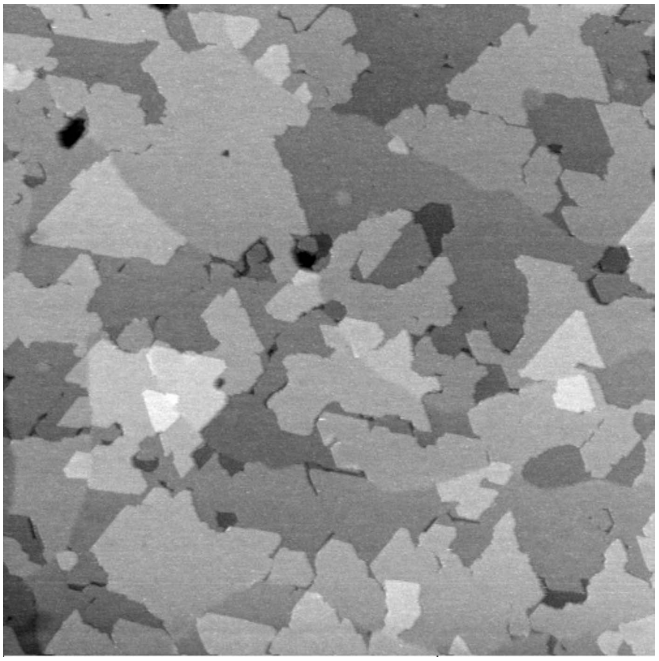

FIG. 1. Surface topography of crystalline ice. This 750 $\times$750 nm^2 STM image shows a continuous 4 nm thick ice film grown onto Pt(111) at 140 K. STM is able to nondestructively investigate ice multilayers and routinely resolve surface steps of bilayer height (3.7 Å).

other techniques. This (often quantitative) agreement provides evidence that our imaging is nondestructive. More importantly, new insights into growth morphology can be obtained. Smooth amorphous films[22] form when the deposition temperature is below 120 K, whereas crystalline ice appears at higher temperatures. The image series in Figs. 2(a)–2(c) shows the surface morphology of ice grown at T=100 K for mean film thicknesses of 1.7, 2, and 20 bilayers (BLs). As expected for amorphous films, there are no discernible regular features besides the relatively straight substrate steps. The striking difference in roughness between the 1.7 BL film [Fig. 2(a)] and the 2 BL film [Fig. 2(b)] clearly reveals that these films start to grow in a layer-by-layer mode, providing a real-space confirmation of the findings of Kimmel *et al.*[23] based on thermal-desorption measurements. The absence of any discernible surface steps on the 20 BL film shown in Fig. 2(c) indicates that the layered structure imposed by the substrate fades away with increasing distance from the substrate.

We now discuss the growth of crystalline ice at 140 K. As reported before,[6,13,17,18] we find that the first layer of water wets the Pt(111) substrate. The wetting layer is depicted in Fig. 3 for the (a) 0.4 BL and (b) 0.95 BL coverages. The 0.4 BL image reproduces the observation of Morgenstern *et al.*[24] that water bonds well to the upper side of Pt(111)-step edges. The 0.95 BL image in Fig. 3(b) shows two depressions. The upper, hexagonal one is a two-dimensional (2D) vacancy island in the Pt substrate covered with the wetting layer. The lower, irregular one is a patch of remaining bare Pt. We were not able to resolve the molecular structure of the wetting layer. The corrugation seen in the images is moirélike with a spacing roughly consistent with a $\sqrt{39}$ spacing but less well ordered than one would expect from previously reported diffraction studies.[13,17] To capture how the film morphology evolves with thickness, we exposed the substrate to a certain amount of water, then cooled it to 110 K for imaging, and repeated this cycle up to a mean film thickness d=9 nm, yielding the image sequence in Figs. 3(c)–3(f). At d =0.8 nm, the film consists of individual 2–3 nm high crystallites embedded in a one bilayer high wetting layer [Fig. 3(c)], corroborating the thermal-desorption measurements of Kimmel *et al.*[18] In a separate paper,[25] we analyzed the annealing behavior of these regular-shaped crystallites and report that their dewetting was limited by the nucleation of new molecular layers on their top facets. Upon deposition of additional 0.7 nm of water (total thickness d=1.5 nm), crystallites coalesce, forming a labyrinthine pattern [Fig. 3(d)] with channels extending down to the wetting layer. At a total thickness of 4 nm, most channels are filled in, leading to larger and up to 300 nm wide atomically flat terraces, on which ice steps are easily recognizable [Fig. 3(e)]. Some

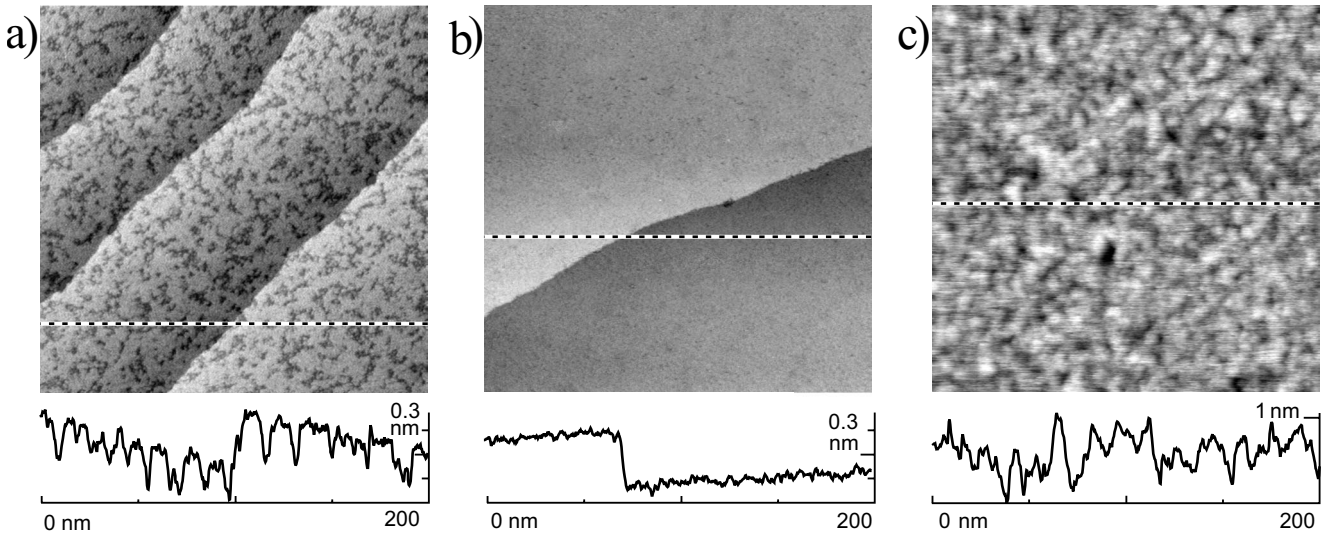

FIG. 2. Surface topography of amorphous ice grown at T=100 K. 200$\times$200 nm^2 STM images showing amorphous ice films for mean film thicknesses of (a) d=1.7, (b) 2, and (c) 20 bilayers (6 nm).

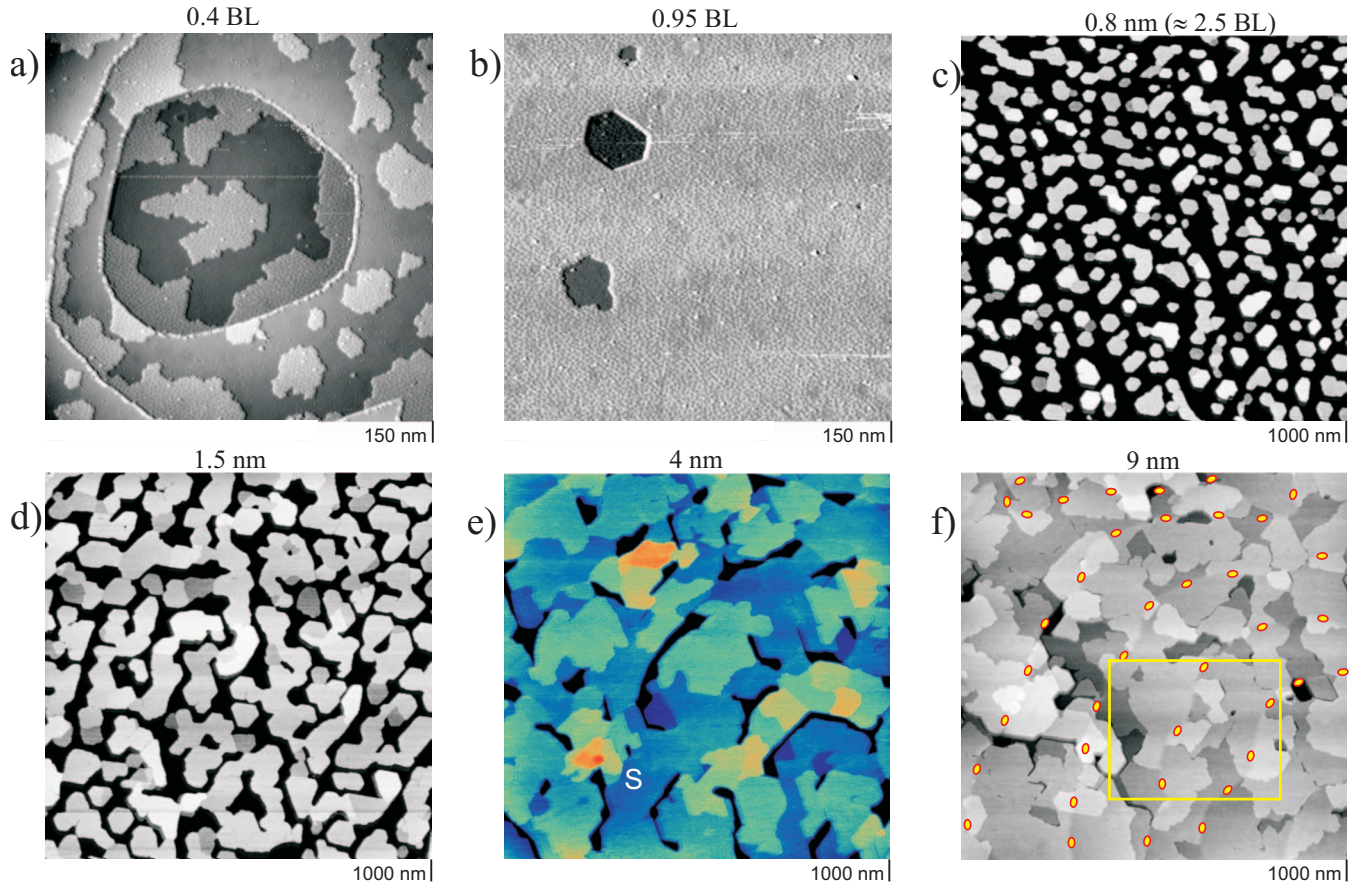

FIG. 3. (Color) Surface topography of crystalline ice grown at 140 K. This image sequence shows the evolution of a crystalline ice film, which was deposited at $T=140$ K, with increasing mean film thickness (indicated above the individual images). [(a) and (b)] 150 $\times 150$ nm^2 STM images of the wetting layer. (c)–(f) 1×1 μm^2 images of multilayer films. In (e), the letter "S" marks a growth spiral, which has formed above a buried substrate step. In (f), the buried substrate steps are marked with yellow-red ellipses. The yellow rectangle marks the area that corresponds to Fig. 5(a).

regions begin to rise above their surroundings, most notably the triangular spiral labeled S. At $d=9$ nm [Fig. 3(f)], the entire area is covered by an ice film of rather uniform thickness (rms roughness=0.4 nm) with the exception of a few remaining pinholes. The trend that some regions grow thicker (higher) continues, and it becomes more obvious that these areas preferentially reside above the buried substrate steps marked yellow-red. As we will discuss later, these regions serve as nuclei for the metastable phase of cubic ice 1c.

Substrate steps, such as the one depicted in Fig. 4(a), strongly influence the properties of crystalline ice films. In Fig. 4(b), which shows a film equivalent to the one in Fig. 3(c), the individual substrate terraces are differently colored. Strikingly, almost none of the ice crystallites cross a substrate step, which has consequences for the structure of thicker (>5 nm) ice films, as described in Sec. IV. At a slightly higher temperature, i.e., 150 K instead of 140 K, the ice crystallites are larger and farther apart. Therefore the growing crystals are more likely to encounter a substrate step before coalescing with a neighboring crystal. Figure 4(c) shows a 3.5×3.5 μm^2 image of such a film of 3 nm average thickness grown at 150 K. The large ice crystallites are elongated along the substrate steps, which circle around a shallow surface protrusion. (Some of the 10 nm high crystals appear twice—an artifact due to a double STM tip.) At larger thicknesses, when ice crystallites have coalesced into a continuous film, the effect of substrate steps is less conspicuous but perhaps more profound, as we will discuss in Sec. IV. Such coalesced films are depicted in Figs. 4(d) and 4(e), which show a 4 nm thick continuous film grown at 140 K, and in Fig. 4(f), showing a 6 nm thick film grown at 145 K, which still contains some open channels. In all three images, the highest surface region is associated with a triangular growth spiral around a screw dislocation. In Figs. 4(d) and 4(e), the substrate steps, which are buried under a continuous film, appear as faint surface height changes, some of which are marked with yellow red ellipses. Almost all growth spirals develop above substrate steps, i.e., Fig. 4(d) represents the typical case and Fig. 4(e) the rare exception. The spiral marked "S" in Fig. 4(f) is in a more advanced stage and has risen high above the surrounding surface region. In Sec. IV, we argue that these spirals are the origin of cubic ice 1c.

IV. FORMATION OF CUBIC ICE

Nucleating molecular layers on the film's surface costs energy because new step edges have to be created, as discussed for ice/Pt in Ref. 25. Crystals can grow while avoiding new layer nucleation if screw dislocations intersect the

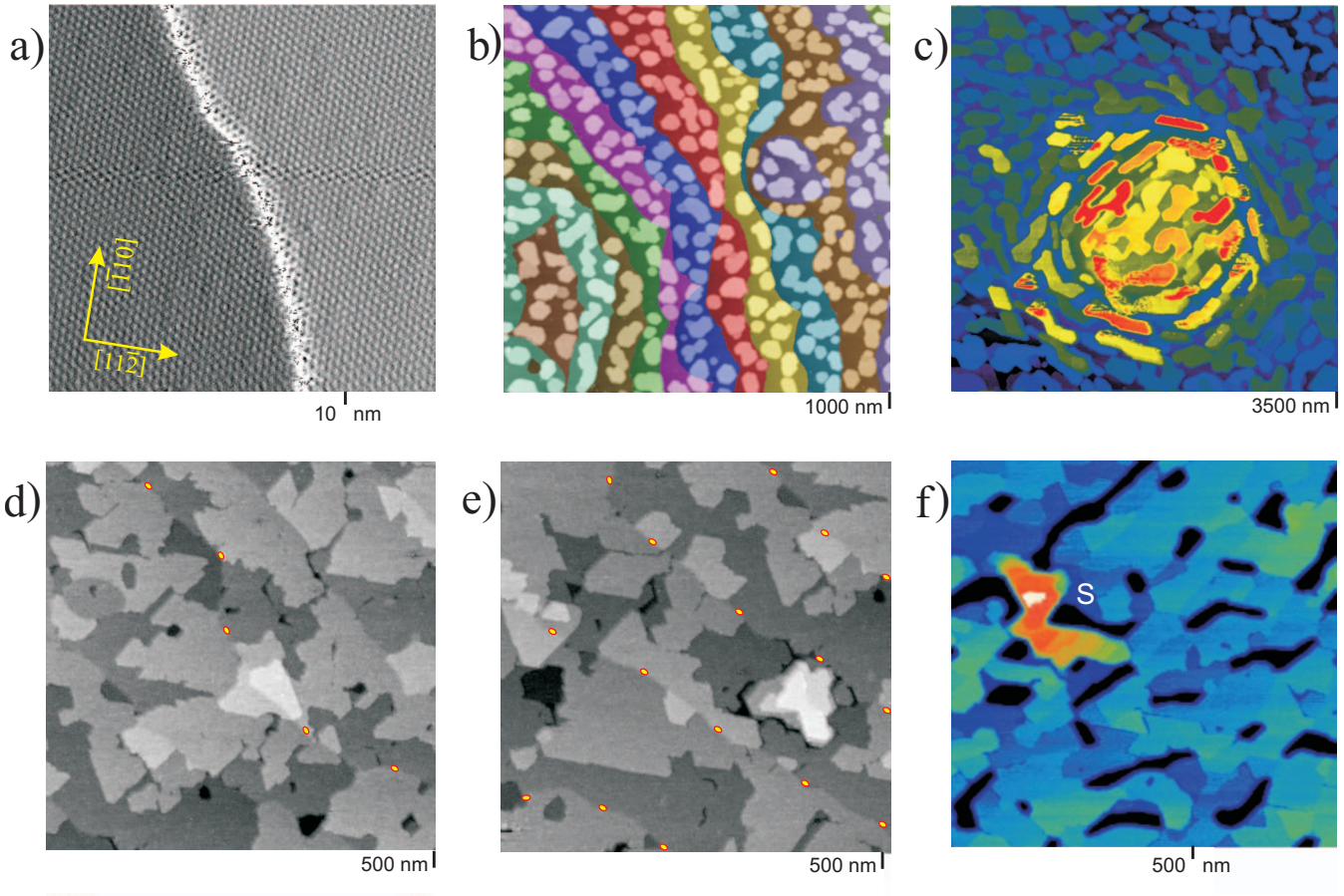

FIG. 4. (Color) Influence of substrate steps on the morphology of crystalline ice films. (a) 13×13 nm^2 STM image of the Pt substrate. The atom positions on both sides of the atomic step are used to obtain the crystallographic orientations of the sample. The crystallographic orientations indicated in the lower left corner are valid for all STM images herein. (b) 1×1 μm^2 STM image of an ice film with a mean thickness of 0.8 nm grown at 140 K. In this image, the individual substrate terraces are colored differently. The ice crystallites avoid crossing a substrate step. (c) Image size: 3.5 μm$\times$3.5 μm; mean thickness: 3 nm; deposition temperature: 150 K. The large elongated crystallites follow the substrate steps, which circle around a shallow surface protrusion. [(d)–(f)] Triangular growth spirals produced by screw dislocations. Most spirals develop above substrate steps (some are marked by yellow ellipses). [(d) and (e)] 4 nm thick film grown at 140 K. (e) Example of a spiral that is not obviously related to a substrate step. (f) 6 nm thick film grown at 145 K. The fastest film growth in this 800×800 nm^2 area had occurred at a growth spiral labeled S.

surface. In the films of Figs. 3(c), 4(b), and 4(c), few, if any, such dislocations exist. However, in thicker films, such as those in Figs. 3(e), 3(f), and 4(d)–4(f), the spiral steps associated with these dislocations are evident. These dislocations are usually in the thickest film regions, consistent with the expected enhanced growth. Interestingly, as seen in Figs. 3(e), 3(f), 4(d), and 4(f), these dislocations are often located above buried substrate steps. We now show that these dislocations form as a consequence of the mismatch in step height between ice and Pt. The existence of these dislocations has a surprising effect on the structure of the ice crystals: it naturally leads to the formation of metastable cubic rather than hexagonal ice.

Figure 5(a), which depicts an enlarged detail in Fig. 3(f), gives a hint why growth spirals develop above buried Pt steps. In the STM images, these buried steps (one is marked with yellow red ellipses) appear as subtle and smooth surface height transitions. Spread out over a width roughly equal to the film thickness of 9 nm, they can easily be distinguished from the abrupt surface ice steps. Notice that these height transitions frequently change their sign along the buried step. Crossing the buried step from left to right, the surface alternates between descending by 0.6 times the ice-step height h_{ice} (profile 1) or ascending by $0.4h_{\mathrm{ice}}$ (profile 2). Considering that the Pt(111)-step height of 2.26 Å is roughly one-half the ice-bilayer spacing (h_{ice}=3.66 Å, $h_{\mathrm{Pt}}=0.62h_{\mathrm{ice}}$) this switching between descending and ascending can be easily understood. Given that $\frac{3}{4}$ of the bonds in bulk ice are intralayer compared to only $\frac{1}{2}$ of the nearest neighbor bonds in fcc(111) and hcp(0001), for instance, the ice layers have a strong tendency to connect across substrate steps despite the energy cost associated with distorting the ice lattice. The energy cost of bending upward by $0.4h_{\mathrm{ice}}$ to connect to the slightly higher layers on the other side [solid lines in Fig. 5(b)] is not much different than if the layers bend downward by $0.6h_{\mathrm{ice}}$ to connect to the other side [dotted lines in Fig. 5(b)]. At the point at the step edge where there is a change between ascending and descending connecting layers, a screw dislocation is created, as shown in Fig. 5(c), leading to the growth spirals we observe.

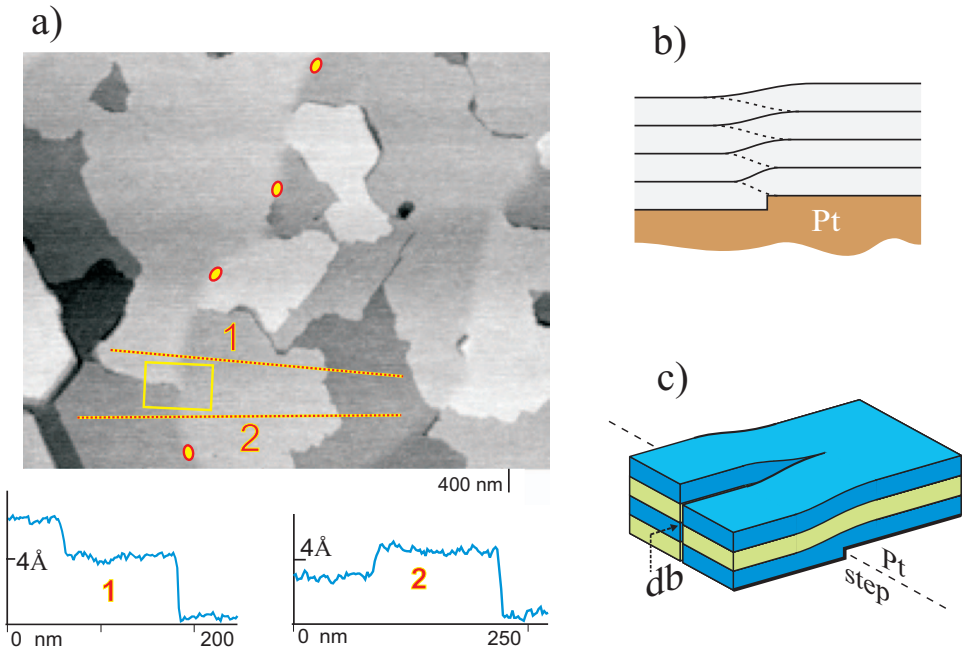

FIG. 5. (Color) Ice layers connecting across a buried substrate step. (a) Enlarged 440×340 nm^2 detail of the 9 nm thick film shown in Fig. 3(f). Crossing the buried Pt step marked by red-yellow ellipses from left to right, the surface either drops (profile 1) or rises (profile 2) by roughly half the ice-bilayer spacing of 3.7 Å. The yellow rectangle marks the area that corresponds to the schematic in (c). [(b) and (c)] Schematics of how ice layers connect across a Pt step. (c) Connecting two domains, separated by the boundary labeled db, to one domain on the other side of a Pt step creates a screw dislocation.

The winding of the spirals associated with these dislocations provides a mechanism for the formation of cubic ice. First, consider the molecular structure of the bilayers. In the naturally occurring crystal phase, ice 1h, oxygen atoms are arranged in puckered honeycomb layers held together by hydrogen bonds[1] [Fig. 6(a)]. Interlayer bonding is accomplished by H bonds between the lower O atoms of the higher layer and the higher O atoms of the lower layer [Fig. 6(b)]. Within a bilayer, each higher oxygen atom binds to three neighboring lower oxygen atoms, forming a triangle. Such triangles can have two orientations that reflect different stackings within the bilayer. The two types of intrabilayer stacking are labeled in Fig. 6 by the green and blue triangles. In the top view, the green triangles point upward and the blue downward. In the equilibrium structure of hexagonal ice 1h [Fig. 6(b)], the stacking alternates between "green" and "blue," whereas in metastable cubic ice 1c[1,2,19] all bilayers are stacked the same way, i.e., either green or blue [Fig.

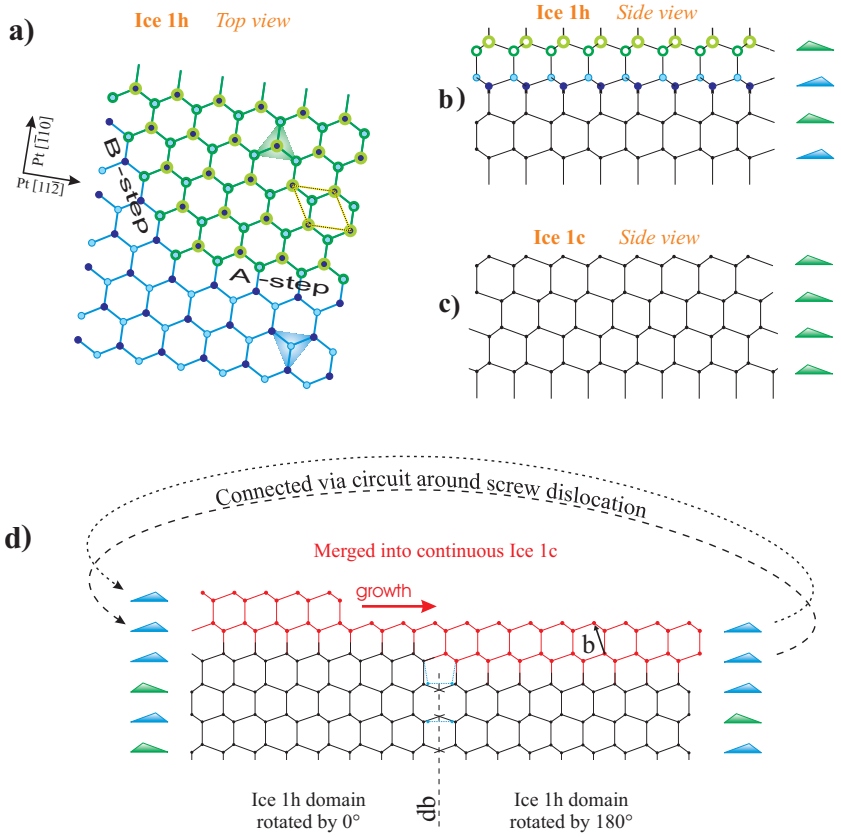

FIG. 6. (Color) Mechanism for cubic ice formation. (a) Schematic top view of an ice bilayer (blue) partially covered by a bilayer (green) bounded by a surface step with A-step and B-step sections. The oxygen atoms (circles) are connected via H bonds (lines). Within each bilayer the higher oxygen atoms are surrounded by three lower-lying oxygen atoms forming triangles (green or blue) whose upward or downward orientation reflects the two possibilities for intrabilayer stacking. [(b) and (c)] Schematic side views of four ice bilayers in the equilibrium hexagonal ice 1h configuration and in the metastable cubic ice 1c configuration. The triangles at the right indicate the intrabilayer stacking. (d) Same configuration as in Fig. 5(c) viewed along the domain boundary db toward the Pt step. Overgrowing the boundary db between two ice 1h domains (black) by new material (red) creates a growth spiral surrounding the screw dislocation with a Burgers vector b.

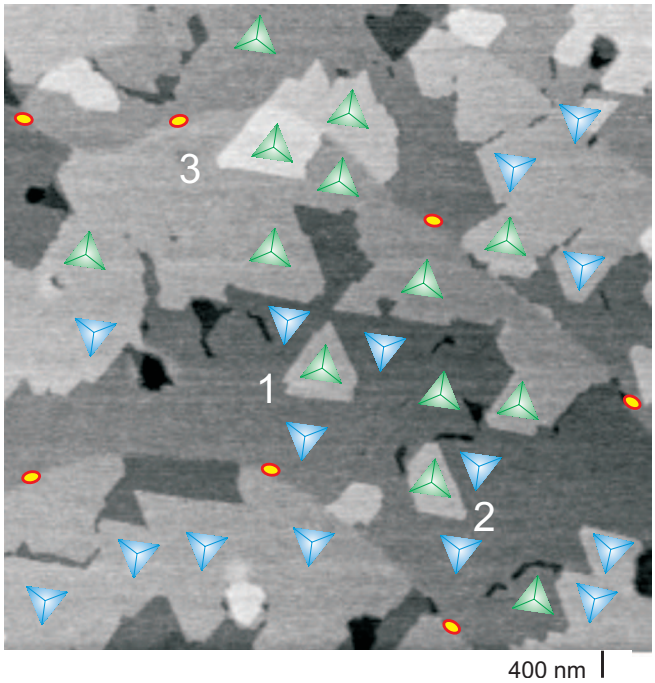

FIG. 7. (Color) STM image of a 4 nm thick ice film. The surface regions are labeled with triangles according to their intrabilayer stacking. Some stacking-domain boundaries appear as small crevices. Two buried substrate steps are marked yellow-red. Nucleating the triangular 2D islands labeled 1 and 2 produced the stacking sequence of hexagonal ice 1h. Ice attaching to a screw dislocation as occurring in the feature labeled 3 leads to the stacking sequence of cubic ice 1c.

6(c)]. The energy difference between these stackings is believed to be small.[26]

Given this structure, we suggest that the decision of bending upward versus downward when two crystals impinge on each other across a Pt-step edge is made in a way that allows the layers to maintain their bilayer stacking through the combined crystal. As a consequence, where a boundary separating domains of opposite bilayer stacking ends at a Pt step, the ice layers connect across the Pt step in a way that produces the screw dislocation discussed above. The small crevices that decorate some of these domain boundaries, as seen in Figs. 5(a), 1, and 7, corroborate this idea—the high energy of domain boundaries would cause these regions of the crystal to fill in more slowly. The configuration in Fig. 5(c), which corresponds to the area marked by a yellow rectangle in Fig. 5(a), represents a growth spiral in its embryonic state. The lower black portion of the lattice schematic in Fig. 6(d) shows this configuration looking down the domain boundary toward the Pt step. The upper red portion shows how the subsequently grown ice has to attach to form a growth spiral. For a spiral to develop, the domain boundary has to be overgrown. If this occurs by extending the existing layer across the domain boundary and conserving its bilayer stacking [blue in Figs. 5(c) and 6(d)], the domain boundary gets buried, effectively eliminating its impeding effect for growing the next layers. A growth spiral has been created; from now on, growth can proceed by simply attaching new material to the existing ice layer, thus propagating its bilayer stacking

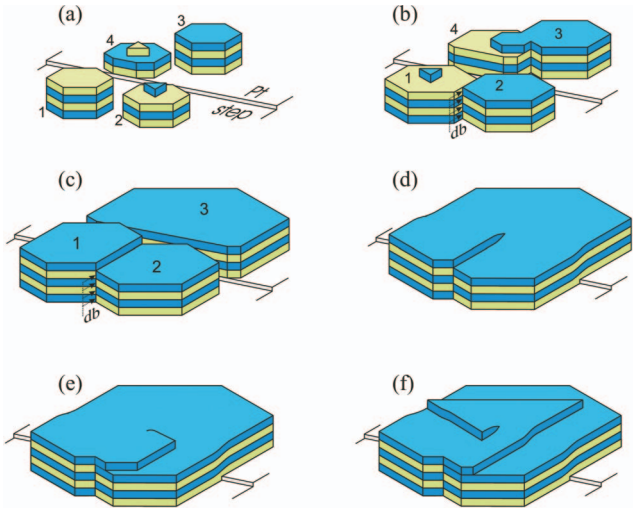

FIG. 8. (Color) Scenario summarizing key processes leading to growth of cubic ice. Individual ice crystals grow (a) and expand laterally until (b) they coalesce or encounter a substrate step (crystal 4). (c) Crystals merge if their bilayer stacking matches or, else, form a domain boundary labeled db. (d) Layers bend upward or downward to join layers of equal intralayer stacking across a substrate step, producing a screw dislocation. After overgrowing the domain boundary, (e) the top layer can easily expand and form a growth spiral (f). Here, ice of uniform intralayer stacking (blue in this case), i.e., cubic ice 1c is being generated.

despite the higher energy of this stacking. Since the new material has a uniform bilayer stacking [blue in the examples in Figs. 5(c) and 6(d)], metastable cubic ice 1c is being produced.

Evidence that this process does occur in our experiments can be obtained by examining the surface step structure of

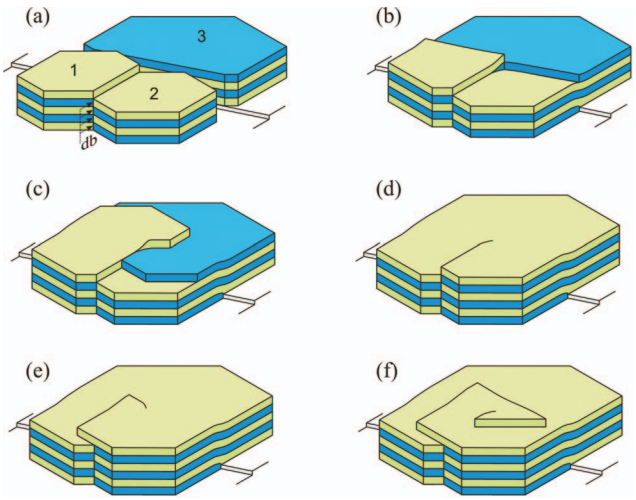

FIG. 9. (Color) Modified scenario with the configuration in (a) being equivalent to that of Fig. 8(c) but with the stackings of crystals 1 and 2 reversed. Now, (b) connecting matching layer across the Pt step creates two surface ice steps in addition to a screw dislocation. [(c) and (d)] The ice layers bounded by these two steps expand. After overgrowing the domain boundary, (e) the top layer starts a growth spiral of opposite chirality and different intralayer stackings (green) than in the scenario of Fig. 8.

the ice films. We often find straight step edges parallel to one of the six directions along which the "ice rings" are close packed (Fig. 7). For a given bilayer, there are two sets of three equivalent step orientations. Along one set, each oxygen atom at the step is bound to three neighboring oxygen atoms [A steps, Fig. 6(a)]. Along the other (B steps), the step oxygen atoms have only two neighboring oxygen atoms. One of these step types will be energetically preferred. A 2D island bound by three preferred steps would adopt a triangular shape determined by its bilayer stacking. Assuming all straight steps are A steps, their orientations can then be used to assign the bilayer stacking of specific surface regions. In Fig. 7, we label the surface regions for which we are able to assign the bilayer stacking without ambiguity. New layers, such as the triangular islands labeled 1 and 2, tend to nucleate with a different bilayer stacking than that of the underlying bilayer on which they grew, which corresponds to the equilibrium ice 1h configuration [Fig. 6(b)]. Another observation is that ice layers often grow across buried substrate steps marked yellow-red while maintaining their stacking. As a consequence, growth spirals that originate from screw dislocations above buried substrate steps produce film regions with a uniform bilayer stacking, corresponding to metastable cubic ice 1c [Fig. 6(c)]. An example of such a spiral is the bright triangular feature labeled 3 in Fig. 7. This is a growth spiral in its nascent stage that produces cubic ice with a green bilayer stacking. Examples of more advanced spirals are: the one in Fig. 4(d) (green stacking), the one labeled s in Fig. 3(e) (green) and the fully developed spiral labeled s in Fig. 4(e) (blue stacking).

The scenarios depicted in Figs. 8 and 9 summarize in sequential order the key processes leading to cubic ice formation during film growth. Figure 8(a) shows four individual ice crystallites, two on each side of a substrate step. For simplicity, we neglect the interaction with other crystallites in the vicinity of the four crystals. Each molecular ice layer is colored green and blue according to its intralayer stacking. We will now follow the evolution of this imaginary configuration upon further water deposition. Incorporating the deposited water, the four ice crystallites grow in all dimensions. At this early stage, the crystals can increase their height only by nucleating new layers on their top facets. Eventually, due to lateral expansion, the crystallites start to coalesce [Fig. 8(b)]. Crystal 4 has encountered a substrate step, which stops the advance of its front side wall. As mentioned in Sec. III and seen in Fig. 4(b), individual crystallites cannot overgrow a Pt(111) step. Crystals 3 and 4, for which the stacking matches, immediately begin to merge. Crystals 1 and 2, which differ in their stackings, form a domain boundary labeled db upon making contact. Such domain boundaries often reveal themselves as small crevices in STM images. In Fig. 8(c), the former crystals 3 and 4 have fully merged (new crystal 3) and reshaped and their front side wall has aligned above the substrate step. The domain boundary between crystal 1 and 2 still persists and prevents the expansion of crystal 1's top layer onto the top facet of crystal 2. Both crystals 1 and 2 have expanded and start to make contact with crystal 3 on the other side of the Pt step. Without much delay crystals 1 and 2 merge with crystal 3 across the substrate step [Fig. 8(d)]. To accomplish continuity of the intralayer stacking (green or blue) across the Pt step, the layers of crystal 1 bend downward and those of crystal 2 upward, resulting in a screw dislocation. In Fig. 8(e), the top layer of crystal 1 has managed to overcome the energy barrier to overgrow the domain boundary. This has created a surface step to which water can easily attach. Subsequent growth mainly occurs by advancing this step, which spirals around the screw dislocation [Fig. 8(f)]. The triangular shape of the spiral reflects the three low energy step directions for the given intralayer stacking (blue in this case). This growth spiral produces ice of uniform intralayer stacking (blue in this case), i.e., cubic ice 1c.

The slightly more complicated scenario in Fig. 9 further illustrates the role of bilayer stacking during coalescence. The configuration in Fig. 9(a) is equivalent to that of Fig. 8(c) but with the stacking of crystals 1 and 2 reversed. Now the layers of crystal 1 have to bend upward and those of crystal 2 downward to connect to crystal 3 across the Pt step. The top layer of crystal 1 and the right-hand half of the top layer of crystal 3 have no layer across the Pt step to connect to, thus forming surface steps above the buried Pt step [Fig. 9(b)]. Easy attachment of water causes these surface steps to advance [Fig. 9(c)], leading to the configuration in Fig. 9(d). This situation is almost identical to that of Fig. 8(d), but now the surface layer has green instead of blue stacking, and the Burgers vector of the screw dislocation is reversed. As in the previous scenario, the top layer has to overgrow the domain boundary before it can advance [Fig. 9(e)] and form a growth spiral [Fig. 9(f)], where cubic ice of green intralayer stacking is being generated. The scenarios in Figs. 8 and 9 are two typical examples representing a large number of possible configurations during coalescence, leading to the rich topography observed in STM images of continuous ice films.

This mechanism of growing cubic ice might operate for other substrates as well, because most metals and a range of other surfaces have $\approx 0.5 h_{\mathrm{ice}}$ high steps. It is possible that there exists an alternative mechanism for the generation of these dislocations. We find that such spirals can also be occasionally created without any obvious relation to substrate steps. An example of such a spiral is shown in Fig. 4(e). We thus propose that this dislocation-based mechanism of ice 1c growth is common in solid substrates. For instance, solid cloud condensation nuclei[27,28] might promote the generation of these dislocations, explaining the occurrence of cubic ice in atmospheric clouds.[29,30] If such dislocation generating nuclei or defects existed in amorphous ice, it would explain why cubic ice forms when amorphous ice is heated as proposed to occur in icy bodies in the outer solar system,[31,32] for example.

V. NONDESTRUCTIVE IMAGING OF ICE MULTILAYERS

The ability to image >3 nm thick ice films seems counterintuitive because STM relies on electrical conductivity and ice is a good insulator.[2] Control experiments with thicker-than-20-bilayer films of crystalline and amorphous ice grown on Pt(111) and Ru(0001) imaged between 60 K and 120 K suggest that this capability is not limited to one particular structure or substrate, but rather seems to be a

general property of ice. How is this possible, given that ice is an insulator? The first clue about the mechanism is that imaging is only possible when the Pt substrate is negatively biased with respect to the tip, i.e., electrons are extracted from the ice, by voltages $V_{sample} < -6(\pm 1)$ V. The experiment depicted in Fig. 10(a) illustrates the dramatic voltage dependence when scanning a 6 nm thick crystalline film. First, a smaller 1×1 μm^2 square is scanned using a positive (+7 V) sample bias. Then, the polarity is reversed (−7 V sample bias) and a larger 2 $\mu m \times 2$ μm area is imaged. The complete destruction of the ice film at a positive sample bias sharply contrasts with the ability to nondestructively image the ice film at a negative sample bias. Figure 10(b) shows the same behavior on a 6 nm thick amorphous film. This observation seems to rule out explanations invoking a highly conductive surface layer in contact with the Pt. However, the threshold voltage of $-(6 \pm 1)$ V for imaging corresponds to the energy of the first occupied states of ice in contact with Pt.[33] This suggests that the electronic levels have the spatial dependence shown in Fig. 10(c). The applied voltage lifts the energy levels of the ice sufficiently with respect to the levels of the tungsten STM tip so that electrons can tunnel through the vacuum gap from the highest occupied H_2O orbital into the empty states of the STM tip. This scenario is plausible (1) if there is little voltage drop across the ice layer and (2) if there is enough conduction through the ice layer to supply the tunneling electrons.

Can the first condition be met if the highly polar water molecules exhibit a preferred orientation? A crude one-dimensional approximation shows that canceling the electric field in ice through polarization might be possible. The typical imaging conditions of $V_{sample} = -7$ V and STM tip-sample distance of 1 nm yield the electrical field in the vacuum gap between the STM tip and ice surface $E_{gap} = 7 \times 10^9$ V/m. The corresponding electric displacement is $D_{gap} = e_0 E_{gap} \approx 0.06$ C/m^2. To eliminate the electric field in the ice film (completely, for simplicity) the polarization of the ice would need to be $P_{ice} = D_{gap} = 0.06$ C/m^2. A configuration that maximizes the polarization along the surface normal while obeying the ice rules[2] is realized in the ice XI structure.[2] Here, the dipole moment of a water molecule projected onto the c axis (i.e., parallel to the surface normal in our experiment) is on average $p^{\parallel}_{H2O} \approx 2.8 \times 10^{-30}$ Cm. With approximately 3×10^{28} water molecules per m^3, the polarization of ice XI is roughly $P_{iceXI} = 3 \times 10^{28}$ m$^{-3} \times 2.8 \times 10^{-30}$ Cm $= 0.084$ C/m^2, which is slightly more than $P = 0.06$ C/m$^2 = D_{gap}$, the polarization necessary to completely cancel the electric field. So, even if possible bond distortions and electronic contributions are not included, the polarization in ice can, in principle, be high enough to effectively reduce the electric field in the ice film. Figure 10(d) shows the situation if the ice film were not polarized enough to reduce the electric field sufficiently within the film. In that case the empty states above E_f in the W tip would not be lined up with any filled states in the ice that are close enough (<2 nm) to have a detectable tunneling probability. Thus, a large polarization of ice seems necessary to explain our ability to nondestructively image ice with STM.

At this point, we can only speculate about the origin of this field-canceling polarization. One possibility is that the

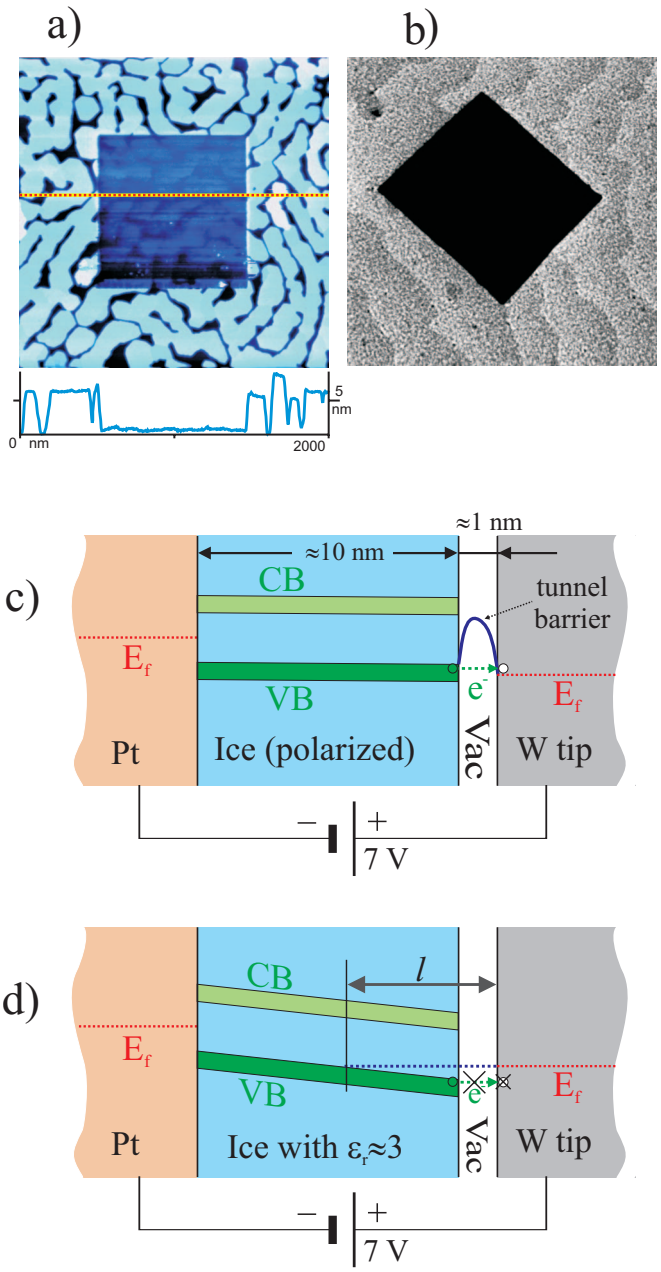

FIG. 10. (Color) Imaging ice-multilayer films on Pt(111). (a) First, the dark 1×1 μm^2 square in the center was carved out by scanning this area with a positively biased sample $V_{sample} = 7$ V injecting electrons into the ice. Then, the STM imaged a larger 2×2 μm^2 area with $V_{sample} = -7$ V, extracting electrons from the ice. (b) shows the same method used on a 6 nm thick amorphous film. Image area: 1×1 μm^2. (c) Schematic of the energy levels for the imaging mode. Due to a strong polarization of the ice, most of the applied voltage drops in the vacuum gap. As a consequence, the highest occupied ice states line up with the lowest empty states of the W tip—a precondition for electrons to tunnel from the sample into the tip. (d) Energy diagram for the case of weak polarization. A significant portion of the voltage drop occurs within the ice film. The shortest distance l for which filled states in the ice line up with empty states in the W tip is too large (>3 nm) for electrons to tunnel through the gap of width l from the ice into the tip.

water molecules are reoriented during the imaging process by the strong electric fields due to the applied tunneling voltage. Since no tip-induced disruption of the film's morphology is observed, this reorientation would have to occur without any detectable mass transport. That is, the water molecules would have to rotate in place, temporarily violating the ice rules during the reorientation process. Alternatively, it is conceivable that the interaction with the substrate imposes a preferred orientation of the water molecules. This scenario is consistent with the surface-induced ferroelectricity of ice/Pt(111) measured with optical sum-frequency vibrational spectroscopy by Su *et al.*[34] Interactions of ice with the substrate could, in principle, also include a buildup of electrical charges due to water dissociation, as reported by Lilach *et al.*[35] However, a measurable charging effect has only been reported for $T>150$ K, which is too high to affect our imaging.

Condition (2), i.e., that ice can supply the tunneling electrons, is interesting because previously the electric DC conductivity of ice had been solely attributed to the migration of protonic defects.[2] For our case, we exclude proton-based mechanisms because even a complete decomposition of the ice film could not supply enough electrons needed for STM. A crude back-of-the-envelope estimate suffices to discard this possibility: Using typical imaging parameters, i.e., scan area $A=1$ μm^2, acquisition time $t\approx 3000$ s, and tunneling current $I=0.35$ pA, the STM passes a charge of $\approx 10^{-9}$ C $\approx 10^{10}$ e through 1 μm^2 of ice surface. Assuming there are approximately ten surface water molecules per nm^2, this corresponds to a flux of ≈ 1000 elementary charges per surface molecule. Since in the experimental setup in vacuum there is neither a sink nor a source for protons other than a possible decomposition of the ice, an electronic transport via protonic defects cannot obviously supply the electrons needed for nondestructive imaging, leaving conduction via electrons in the depleted highest occupied orbital as the most plausible mechanism. Still, much uncertainty remains. Nevertheless, our results provide motivation for more thorough studies of electrical transport in ice films.

In typical STM experiments, sample voltages of $|V_{sample}|<4$ V are common. In this case, the imaging mechanism described above is not active, and the STM tip, seeking to maintain the set tunneling current, moves closer toward the substrate. Consistent with this scenario, we observe that at these voltages, the STM tip always destructively interacts with ice films of more than 2–3 bilayers thickness. Figure 11 illustrates such a tip-sample interaction. At a sample bias of −0.9 V and the tunnel current gradually ramped up from 0.7–1.2 pA, the STM tip gradually scrapes away the uppermost bilayer of a 3 bilayer high ice crystal. The asymmetry of the scraping—the crystal is preferentially attacked on the left side—indicates that the tip condition is at least as important as the exact values of tunnel current and scan time. The crystal left behind [Fig. 11(c)] exhibits a top layer decorated by a triangular array of small protrusions presumably reflecting a moiré between Pt(111) and the ice lattice. Upon reducing I_{tunnel} to 0.5 pA, the top layer spontaneously regrew even at 120 K, starting with triangular nuclei [Fig. 11(d)]. Cleanly scraping away a complete layer without destroying the entire crystal might be facilitated by the fact that only $\frac{1}{4}$ of the bonds in bulk ice are interlayer, compared to $\frac{1}{2}$ of the nearest neighbor bonds in fcc(111) and hcp(0001).

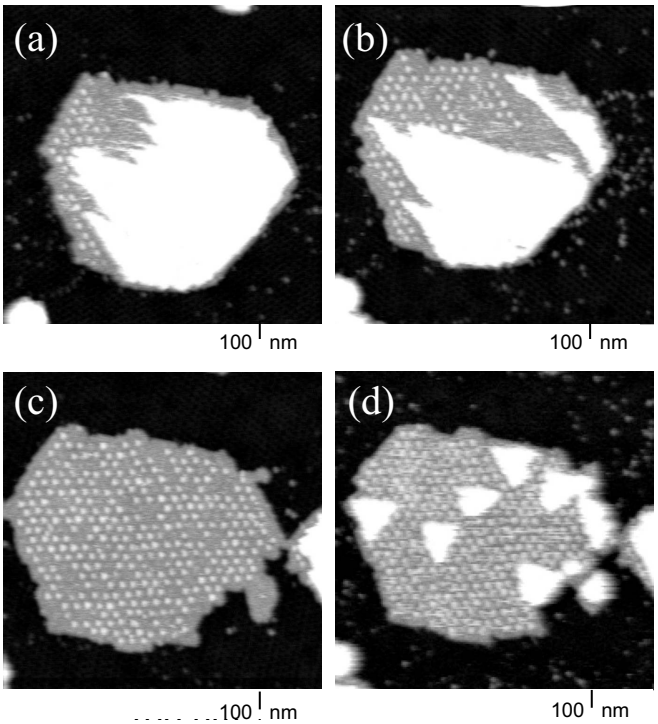

FIG. 11. Tip-induced removal and spontaneous regrowth of a molecular ice layer. At a sample bias of $V_{sample}=-0.9$ V and a tunnel current I_{tunnel} ramped from 0.7–1.2 pA, the STM tip scrapes away the uppermost bilayer of a three bilayer high ice crystal. The time sequence [(a)–(c)] shows the cumulative result of continuous scanning across the imaged crystal. The images were acquired (a) after 30 min scanning at $I_{tunnel}=0.7$ pA. (b) After additional 20 min scanning at $I_{tunnel}=0.8$ pA and (c) after one more hour at $I_{tunnel}=1.2$ pA. (d) Upon reducing I_{tunnel} to 0.5 pA, the top layer spontaneously started to regrow.

VI. SUMMARY

We have established that STM can be used to nondestructively image ice multilayers. We suggest that the imaging relies on the high polarizability of ice, allowing the STM tip to extract valence electrons from the ice. Exploiting this advance, we obtain real-space information about how amorphous and crystalline ice films evolve during growth. Substrate steps play a defining role in the morphology and structure of crystalline ice films. In particular, these steps promote the creation of screw dislocations in thicker films. Finding that growth spirals around these screw dislocations produce cubic ice 1c, we uncovered a mechanism that explains at a molecular level why cubic ice is often observed during growth on substrates at low temperatures. In light of Vonnegut's famous proposal[36] that rapid nucleation of ice crystals by AgI is caused by the similarities of their crystal lattices, it is perhaps amusing to note that we find that fast ice growth on Pt is promoted by a large mismatch in step heights.

ACKNOWLEDGMENTS

We are grateful to C. B. Carter, P. J. Feibelman, F. Leonard, R. Stumpf, and J. Sugar for valuable discussions. This research was supported by the Office of Basic Energy Sciences, Division of Materials Sciences, U.S. Department of Energy under Contract No. DEAC04-94AL85000.

[1] P. V. Hobbs, *Ice Physics* (Clarendon, Oxford, 1974).
[2] V. F. Petrenko and R. W. Whitworth, *Physics of Ice* (Oxford University Press, Oxford, 1999).
[3] F. C. Frank, Contemp. Phys. **23**, 3 (1982).
[4] J. Y. Tsao, *Materials Fundamentals of Molecular Beam Epitaxy* (Academic, San Diego, 1993).
[5] A. Verdaguer, G. M. Sacha, H. Bluhm, and M. Salmeron, Chem. Rev. (Washington, D.C.) **106**, 1478 (2006).
[6] M. Morgenstern, J. Muller, T. Michely, and G. Comsa, Z. Phys. Chem. **198**, 43 (1997).
[7] A. Michaelides and K. Morgenstern, Nat. Mater. **6**, 597 (2007).
[8] M. Mehlhorn and K. Morgenstern, Phys. Rev. Lett. **99**, 246101 (2007).
[9] V. N. Vertsner and G. S. Zhdanov, Sov. Phys. Crystallogr. **10**, 715 (1965).
[10] I. Baker, Microsc. Res. Tech. **62**, 70 (2003).
[11] M. A. Henderson, Surf. Sci. Rep. **46**, 1 (2002).
[12] G. A. Kimmel, N. G. Petrik, Z. Dohnalek, and B. D. Kay, Phys. Rev. Lett. **95**, 166102 (2005).
[13] S. Haq, J. Harnett, and A. Hodgson, Surf. Sci. **505**, 171 (2002).
[14] G. Zimbitas, S. Haq, and A. Hodgson, J. Chem. Phys. **123**, 174701 (2005).
[15] G. Zimbitas and A. Hodgson, Chem. Phys. Lett. **417**, 1 (2006).
[16] N. Materer, U. Starke, A. Barbieri, M. A. VanHove, G. A. Somorjai, G. J. Kroes, and C. Minot, Surf. Sci. **381**, 190 (1997).
[17] A. Glebov, A. P. Graham, A. Menzel, and J. P. Toennies, J. Chem. Phys. **106**, 9382 (1997); A. Glebov, A. P. Graham, A. Menzel, J. P. Toennies, and P. Senet, *ibid.* **112**, 11011 (2000).
[18] G. A. Kimmel, N. G. Petrik, Z. Dohnalek, and B. D. Kay, J. Chem. Phys. **126**, 114702 (2007).
[19] F. V. Shallcross and G. B. Carpenter, J. Chem. Phys. **26**, 782 (1957).
[20] H. Konig, Z. Kristallogr. **105**, 279 (1944).
[21] G. P. Johari, J. Chem. Phys. **122**, 194504 (2005).
[22] J. M. K. Donev, Q. Yu, B. R. Long, R. K. Bollinger, and S. C. Fain, J. Chem. Phys. **123**, 044706 (2005).
[23] G. A. Kimmel, N. G. Petrik, Z. Dohnalek, and B. D. Kay, J. Chem. Phys. **125**, 044713 (2006).
[24] M. Morgenstern, T. Michely, and G. Comsa, Phys. Rev. Lett. **77**, 703 (1996).
[25] K. Thürmer and N. C. Bartelt, Phys. Rev. Lett. **100**, 186101 (2008).
[26] T. Hondoh, T. Itoh, S. Amakai, K. Goto, and A. Higashi, J. Phys. Chem. **87**, 4040 (1983).
[27] R. R. Rogers and M. K. Yau, *A Short Course in Cloud Physics* (Pergamon, Oxford, 1989).
[28] H. R. Pruppacher and J. D. Klett, *Microphysics of Clouds and Precipitation*, 2nd ed. (Oxford University Press, New York, 1997).
[29] M. Riikonen, M. Sillanpaa, L. Virta, D. Sullivan, J. Moilanen, and I. Luukkonen, Appl. Opt. **39**, 6080 (2000).
[30] B. J. Murray, D. A. Knopf, and A. K. Bertram, Nature (London) **434**, 202 (2005).
[31] D. Prialnik and A. Bar-Nun, Astron. Astrophys. **258**, L9 (1992).
[32] P. Gronkowski, Astron. Nachr. **328**, 126 (2007).
[33] W. Ranke, Surf. Sci. **209**, 57 (1989).
[34] X. Su, L. Lianos, Y. R. Shen, and G. A. Somorjai, Phys. Rev. Lett. **80**, 1533 (1998).
[35] Y. Lilach, M. J. Iedema, and J. P. Cowin, Phys. Rev. Lett. **98**, 016105 (2007); G. Zimbitas, M. E. Gallagher, S. Haq, and A. Hodgson, *ibid.* **99**, 109601 (2007).
[36] B. Vonnegut, J. Appl. Phys. **18**, 593 (1947).